Research Article | Vol. 29, No. 12 / 7 June 2021 / Optics Express 18437
Optics EXPRESS

Rapid prototyping of a bispectral terahertz-to-infrared converter

ARTHUR SALMON AND PATRICK BOUCHON*

DOTA, ONERA, Université Paris Saclay, F-91123 Palaiseau, France
*patrick.bouchon@onera.fr

Abstract: Conversion of terahertz radiation into thermal radiation is a promising approach for the development of low cost terahertz instruments. Here, we experimentally demonstrate bispectral terahertz-to-infrared conversion using metamaterials fabricated using a rapid prototyping technique. The converter unit cell is composed of two metal-insulator-metal (MIM) antennas absorbing independently the terahertz radiation at 96 and 130 GHz and a thin carbon nanotubes (CNT) layer used as a thermal emitter. The converter unit cell has a typical $\lambda/100$ thickness and sub-wavelength lateral dimensions. The terahertz absorption of the converter was observed by monitoring its thermal emission using an infrared camera. Within the first hundred milliseconds of the terahertz pulse, thermal radiation from the CNTs only increases at the location of the MIM antennas, thus allowing to record the terahertz response of each MIM antenna independently. Beyond 100 ms, thermal diffusion causes significant cross-talk between the pixels, so the spectral information is more difficult to extract. In a steady state regime, the minimum terahertz power that can be detected is 5.8 μW at 130 GHz. We conclude that the converter provides a suitable low-cost solution for fast multi-spectral terahertz imaging with resolution near the diffraction limit, using an infrared camera in combination with a tunable source.

1. Introduction

The development of compact and efficient uncooled terahertz instrumentation is necessary to promote the practical applications of terahertz imaging in non destructive testing [1], art conservation [2], archaeology [3], medical diagnosis [4–6] and observation in degraded visual environment [7,8]. These applications mainly originate from *(i)* the high penetration depth of the terahertz radiation through dielectric and non polar materials, and *(ii)* the wide range of chemicals exhibiting absorption features in this spectral range, *e.g.* explosives [9], drugs [10], tissues [11]. In addition, terahertz radiation is non-ionizing, so it is considered safe for use on the human body [12].

Terahertz imaging was initially demonstrated using time-domain spectroscopy (THz-TDS) technique [13–15], which is based on the generation and detection of a broadband terahertz pulse using two photoconductive antennas excited by a femtosecond laser [16]. This technique provides phase, spectral, and polarimetric information on the observed samples [17]. However, THz-TDS is a single point measurement, so pixel-by-pixel acquisition using a raster scan system is required to record an image. This time-consuming procedure prevents the use of THz-TDS for real-time imaging. Moreover, the observation area is spatially limited by the travel range of the raster scan.

These issues can be overcome by using broadband cameras, *e.g.* microbolometers [18–20], field effect transistor (FET) - based cameras [21–23], in combination with terahertz sources, *e.g.* IMPATT diodes, quantum cascade lasers, for active terahertz imaging [15]. This option is accessible because compact and uncooled terahertz cameras and sources are commercially available. Recently multispectral terahertz cameras based on these technologies have been developed to demonstrate selective detection of explosives [24], pesticides and drugs [25].

Another THz detection approach consists in extending the accessible spectral range of infrared cameras by inserting a thin terahertz-to-infrared converter between the observation area and the

#426138 https://doi.org/10.1364/OE.426138
Journal © 2021 Received 25 Mar 2021; revised 6 May 2021; accepted 11 May 2021; published 27 May 2021

Optics EXPRESS

infrared sensor. In this way, the converter is designed independently from the mature infrared detection scheme. THz-to-IR conversion has been demonstrated in multiple reports [26–30], and frequency selective surfaces (FSS) were used to convert several spectral bands for multispectral imaging [31]. In the latter report the unit cell of the converter was composed of four FSS made of split-ring resonators arrays, absorbing each a radiation band at a specific polarization state. The addition of absorption bands compromised the spatial resolution of the detection because the size of the unit cell size was larger than the wavelength of the incident light.

In this letter, a bi-spectral terahertz-to-infrared converter is designed, fabricated and characterized. The unit cell of the converter is composed of two sub-wavelength antennas absorbing the incident light at 96 GHz and 130 GHz thus allowing diffraction-limited multispectral imaging. At each frequency, the incoming wave is converted into heat in the vicinity of the antenna, in a volume with subwavelength dimensions. In spite of the heat conduction in the membrane, we show that the corresponding thermal emission remains spatially bounded up to a few hundred milliseconds, thus limiting the crosstalk between the two frequencies. The converter is fabricated using a low cost and flexible rapid prototyping technique based on a microplotter system.

2. Design and fabrication

Efficient THz-to-IR conversion requires high terahertz absorptivity and high infrared emissivity in a volume as small as possible. Spectral and polarization selectivity can be achieved by implementing metamaterial absorbers [32] on the converter side exposed to the terahertz light. The resonances of the metamaterial absorbers can be tuned independently to match the spectral bands of interest. However the arrangement of the multispectral converter results from a trade-off between the number of absorption bands and spatial resolution.

Figure 1 shows the structure of the bispectral converter. The membrane is composed of terahertz pixels made of square Metal-Insulator-Metal (MIM) antennas [33] coupled with a thin layer of carbon nanotubes deposited under the metallic layer which acts as the thermal emitter. The MIM antenna is composed of a metallic patch on top of an insulator layer and a metallic layer, thick enough to be considered as infinite. This antenna acts as a Fabry-Perot resonator for the mode propagating in the cavity formed below the metallic patch, and exhibits a nearly total absorption at its first order wavelength, given by:

$$\lambda_{res} = 2n_{\text{eff}}w + \lambda_{\phi}. \tag{1}$$

where w is the width of the top metallic structure, n_{eff} is the effective index of the mode in the MIM cavity and λ_{ϕ} a parameter depending on the phase reflections in the cavity. Other models based on equivalent nanocircuits can accurately predict the resonant frequency of MIM structures [34]. The absorption is insensitive to the polarization of the incident radiation because of the square geometry of the MIM antenna [33]. The converter is arranged as a periodic 2D array of pairs of MIM antennas, as shown in Fig. 1. The widths of the antennas inside a pair equal $w_1 = 920 \pm 5$ µm and $w_2 = 645 \pm 5$ µm. The gap distance between the antennas equals 570 µm in order to prevent possible coupling between the antennas.

The top metallic grating of the MIM antenna was printed using a microplotter system (Sonoplot, Microplotter II) on a 25 µm thick polyimide film (Kapton HN) metallized with 30 nm of aluminum (Sigma Aldrich). A dispersion of silver nanoparticles in diethylene glycol (Novacentrix JSADEV-N291) was used as the metallic ink and sintered on a hot plate for 10 minutes at 220 °C. The printing procedure was detailed previously [35]. A solution of single-walled carbon nanotubes (SWCNT) in water (1 g/L, 1 wt% Triton X-100, Sigma Aldrich) synthesized by the CoMoCat process, was ultrasonicated for 5 minutes and deposited on the aluminum side of the polyimide film by drop casting. Figure 1(e) shows the infrared emissivity of the carbon nanotubes layer measured by Fourier-transform infrared (FTIR) spectroscopy (Bruker, Vertex 70v). The absorptivity $\alpha(\lambda)$ was obtained from the FTIR reflectivity spectrum

Optics EXPRESS

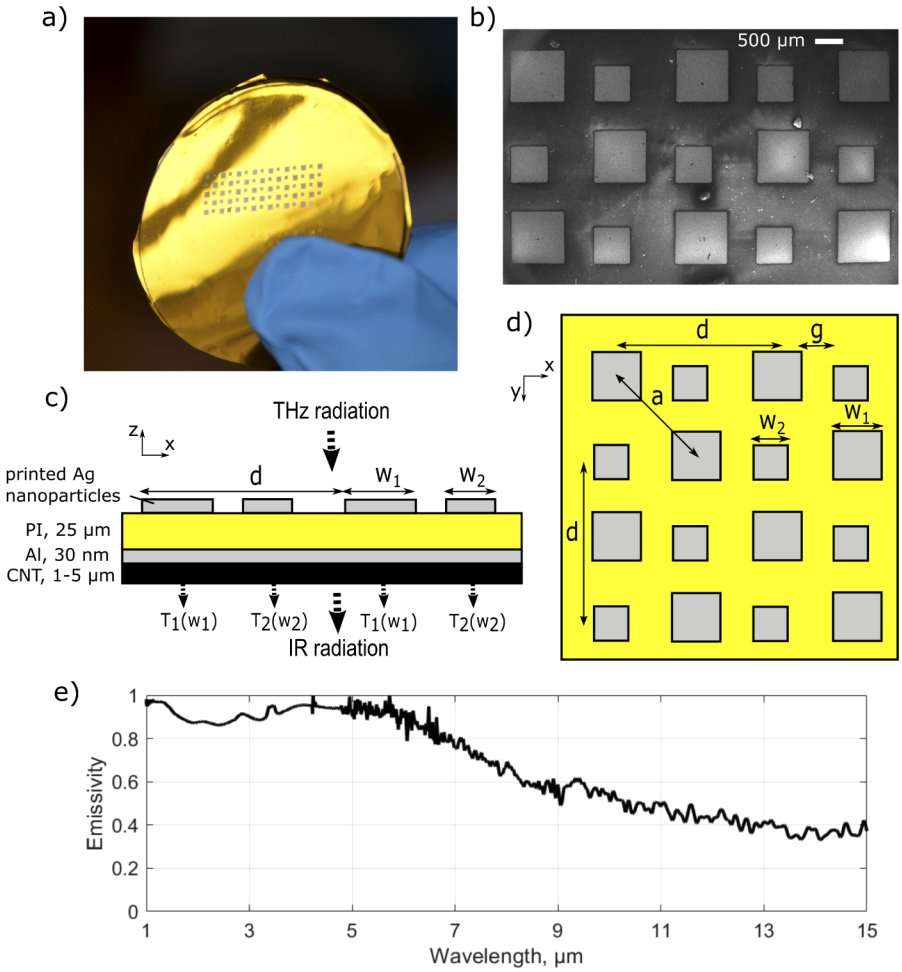

Fig. 1. (a) Photograph of the bispectral converter. (b) Scanning electron micrograph of the antennas. (c) Scheme of a cross section and (d) a top view of the structure. (e) Emissivity spectrum of the CNT layer measured from FTIR reflectivity spectrum at 13° incidence. w_1 = 920 µm, w_2 = 645 µm, d = 3000 µm, $a = d/\sqrt{2}$, g = 570 µm, PI: polyimide, Al: aluminum, CNT: carbon nanotubes

Optics EXPRESS

using the equation $\alpha(\lambda) = 1 - R(\lambda)$, and the emissivity $\epsilon(\lambda)$ was inferred from Kirchhoff's law: $\epsilon(\lambda) = \alpha(\lambda)$. The average emissivity of the SWCNTs equals 0.95 between 1.5 and 5.1 μm (band II), and 0.5 between 8 and 12 μm (band III).

The resonance frequencies were computed using a two-dimensional rigorous coupled wave analysis (2D-RCWA) method. The model was successfully used to predict the resonances of MIM gratings printed by the microplotter in our previous work [35]. A Drude model with the parameters of Ordal *et al.* [36] was used to describe the metallic layers of the antenna, while the dielectric constant of the polyimide equals $\epsilon = 3.1 + 0.05i$ [37,38] between 0.2 and 2.5 THz [39,40]. Figure 2(a) shows the calculated absorptivity spectrum of the designed structure. Two absorption peaks are present at 92.5 GHz and 131 GHz. Dotted lines show the absorptivity spectrum of each MIM antenna. They indicate that the two antennas have little influence on each other. The peak absorptivity of antennas 1 and 2 reach 68 % and 55 % respectively. The total-absorption predicted for MIM antennas could not be reached because of the dissipation in the polyimide layer which broadens the absorption profile and lowers the peak absorption. To reach a higher absorption, the thickness of the film should be increased, but it would be at the expense of the thermal behavior and time response of the THz to IR converter. Figure 2(b) shows the dissipation maps in a cross section of the structure at the two resonance frequencies. At both resonance frequencies, 40 % of the absorption loss is located in the top metallic grating, 57 % in the polyimide insulator, and 3 % in the 30 nm thick aluminum layer.

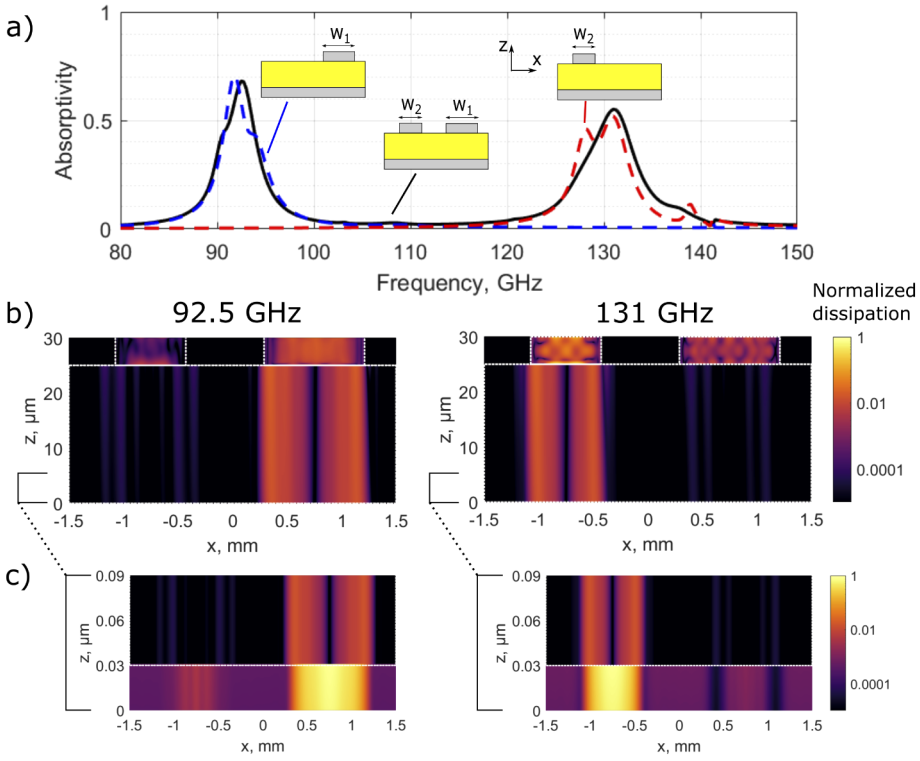

Fig. 2. (a) Calculated absorptivity of the bispectral converter. Dotted blue and red lines show the contribution of individual MIM antennas 1 (w_1) and 2 (w_2) respectively. (b) Normalized dissipation maps in a cross section of the structure at the resonance frequencies of antennas 1 and 2 at F_1 = 92.5 GHz and F_2 = 131 GHz respectively. (c) Zoom of the dissipation map around the 30 nm thick aluminum layer.

Optics EXPRESS

Figure 3 depicts the experimental setup used to investigate the bispectral conversion of the sample. An IMPATT diode (Terasense, P_{out} = 96 mW at 96 GHz), and a Schottky diode pumped by a tunable amplified microwave synthesizer (Lytid, P_{out} = 50 mW at 130 GHz) were alternatively used to illuminate the sample at 96 GHz and 130 GHz respectively. A set of two polytetrafluoroethylene (PTFE, Teflon) lenses collected and focused the terahertz radiation on the converter inserted in a vacuum cell equipped with polymethylpentene (3.5 mm thick, TPX) and potassium bromide (3 mm thick, KBr) windows on the teraherz and infrared sides respectively. The infrared thermal radiation between 1.5 and 5.1 μm was collected by an infrared camera (FLIR systems, SC7600) equipped with a 25 mm objective.

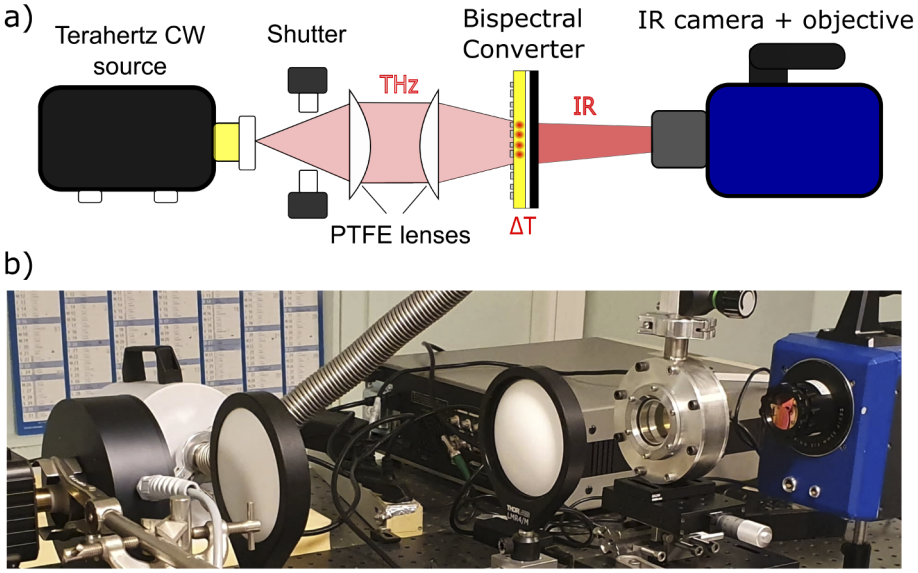

Fig. 3. (a) Schematic and picture of the optical setup used to investigate the bispectral conversion. The terahertz radiation from an IMPATT diode is collected and focused on the THz-to-IR converter using a set of two PTFE lenses. The converter is placed inside a vacuum cell. An infrared camera collects the thermal infrared radiation on the other side of the converter. (b) Photograph of the experimental setup.

3. Results and discussion

The infrared response of the converter to a terahertz beam at 130 GHz focused on the antennas is shown in Fig. 4. The infrared image depicts hot spots corresponding to the local temperature increase due to the terahertz absorption of the MIM antennas. The background was substracted from the images in order to visualize accurately the temperature increase of the MIM antennas. The normalized profile along the x-axis shows that the shape of the beam is approximately gaussian. Using a calibrated uncooled microbolometer (Fluke, Tir), the maximum temperature increase at the center of the beam was estimated to be 19 K. Taking into account the transmission of the PTFE lenses and TPX window, the total power received by the antennas equals 13.6 mW. Assuming a gaussian beam profile, the power captured in the cross section $d^2/2$ = 4.5 mm^2 of the central antenna equals 4.1 mW, so the temperature increase of the converter per unit of incident power equals 3400 K/W. The noise equivalent temperature difference (NETD) of the infrared camera used here equals 20 mK, so the minimum terahertz power that can be detected using the system equals 5.8 μW at 130 GHz.

Optics EXPRESS

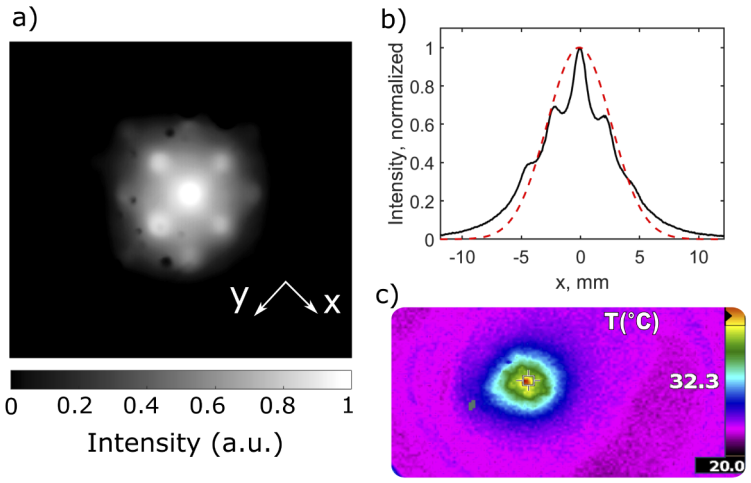

Fig. 4. Terahertz beam profile recorded by the converter at 130 GHz. (a) Infrared image of the converter after background substraction. (b) Intensity profile along the x-axis fitted with a gaussian. (c) Infrared image recorded with an uncooled microbolometer.

Figure 5(a) shows infrared images on a gray scale recorded at 50 Hz during a terahertz pulse at 96 GHz and 130 GHz. The acquisition parameters are the same for both series of images. The images depict the local temperature increase at the location of the terahertz MIM antennas whose resonance frequency matches the frequency of the incident light. Figure 5(b) shows the intensity profiles of each image along the x-axis (shown on the top left image). The sum of the profiles recorded at the two operation frequencies is also plotted in order to retrieve the experimental conditions where the two sources are superimposed on the converter. The graphs show that at the beginning of the terahertz pulse, the infrared signal successfully represents the terahertz response of each MIM antenna. However, beyond 100 ms within the terahertz pulse, the cross-talk between antennas becomes dominant. The origin of the cross-talk can be explained as follows: heat generated by the absorption of the antennas is partially transferred by thermal conduction towards the neighbouring antennas. These neighbors, when heated, emit a IR flux that does not originate directly from the terahertz flux incoming on these antennas. This effect makes difficult the extraction of spectral terahertz information from the images acquired at timescale above 100 ms.

In order to reduce the cross-talk, one should note that the thermal conductivity of carbon nanotubes is extremely variable, *i.e.* from 0.1 to 6600 $W^{-1}m^{-1}K^{-1}$, [41] depending on the number of walls, the orientation and the density of the CNT layer. Here, the SWCNTs form randomly oriented mats, so the thermal conductivity equals about 18 $W^{-1}m^{-1}K^{-1}$, [42] which is two orders of magnitude higher than the thermal conductivity of the polyimide insulator, *i.e.* $\lambda_{th} = 0.13$ $W^{-1}m^{-1}K^{-1}$. Patterning the metallic mirror and CNT layer would strongly reduce the lateral heat conduction flux and thus the cross-talk. In this configuration, the thermal diffusivity D of the converter in the gap between two pixels can be reduced to the diffusivity of the polyimide insulator. Therefore, the thermal diffusion time constant $\tau = D/g^2$, across the gap $g = 570$ µm between two antennas equals about 4.2 s. On the other hand, reducing the lateral dimensions of the metallic mirror would reduce the terahertz absorption. Therefore, there is a trade-off between the efficiency of spectral conversion and the reduction of the cross talk effect.

Optics EXPRESS

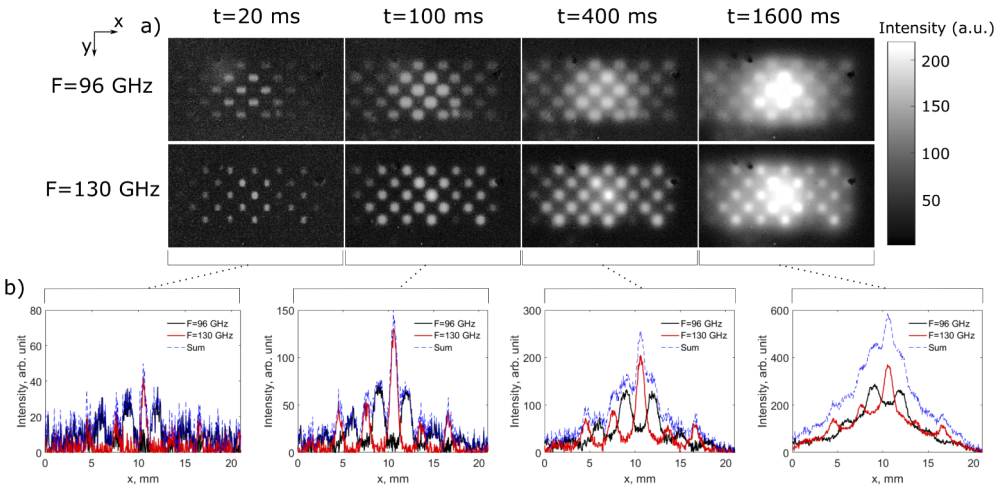

Fig. 5. Temporal dynamic of the bispectral converter. (a) Infrared images of the sample at various times *t* after turning on the terahertz source at 96 GHz and 130 GHz. (b) Infrared intensity profiles along the x-axis at 96 GHz (black) and 130 GHz (red). The sum of the profiles is also plotted (dashed blue). Exposure time = 2 ms, acquisition rate = 50 Hz, single shot.

4. Conclusion

In summary, we have demonstrated bi-spectral terahertz-to-infrared conversion using MIM antennas coupled with a CNT layer. The unit cell of the converter is composed of two MIM antennas absorbing independently the terahertz radiation at 96 GHz and 130 GHz. The antennas were fabricated with a low-cost rapid prototyping method which allows a fine adjustment of the terahertz bands that need to be captured, without the need of photomasks or molds. Infrared imaging shows that the thermal emission profile fairly reproduces the terahertz beam profile. From the thermal emission, the terahertz response of each MIM antenna can be recorded independently at the early stage of a terahertz pulse (< 100 ms). At this stage, bi-spectral terahertz imaging can be performed with a resolution near the diffraction limit. However, beyond 100 ms, thermal diffusion across the CNT layer overlaps the responses of the neighboring antennas. This cross-talk effect prevents the use of the converter for steady-state multispectral imaging. One way to minimize the cross talk would be to pattern the metallic mirror and CNT layer, but additional efforts are required to achieve this by rapid prototyping. The converter efficiency may be further improved by *(i)* using other geometries of antennas in order to reach total terahertz absorption [43,44], and *(ii)* implementing the infrared detector in the near-field of the CNT emitters in order to enhance the radiative heat transfer [45]. We conclude that the multi-spectral converter is a flexible and low-cost system that can be used in combination with pulsed terahertz sources for multispectral imaging using mature infrared cameras.

Funding. Agence Nationale de la Recherche (ANR-10-LABX-0035, ANR-10-LABX-0039-PALM).

Disclosures. The authors declare no conflicts of interest.

Data availability. Data underlying the results presented in this paper are not publicly available at this time but may be obtained from the authors upon reasonable request.

References

1. D. Suzuki, S. Oda, and Y. Kawano, "A flexible and wearable terahertz scanner," Nat. Photonics **10**(12), 809–813 (2016).
2. M. Picollo, K. Fukunaga, and J. Labaune, "Obtaining noninvasive stratigraphic details of panel paintings using terahertz time domain spectroscopy imaging system," J. Cult. Herit. **16**(1), 73–80 (2015).

Optics EXPRESS

3. J. B. Jackson, J. Labaune, R. Bailleul-Lesuer, L. d'Alessandro, A. Whyte, J. W. Bowen, M. Menu, and G. Mourou, "Terahertz pulse imaging in archaeology," Front. Optoelectronics **8**(1), 81–92 (2015).
4. I. Kašalynas, R. Venckevičius, L. Minkevicius, A. Sešek, F. Wahaia, V. Tamošiūnas, B. Voisiat, D. Seliuta, G. Valušis, A. Švigelj, and J. Trontelj, "Spectroscopic terahertz imaging at room temperature employing microbolometer terahertz sensors and its application to the study of carcinoma tissues," Sensors **16**(4), 432 (2016).
5. X. Yang, X. Zhao, K. Yang, Y. Liu, Y. Liu, W. Fu, and Y. Luo, "Biomedical applications of terahertz spectroscopy and imaging," Trends Biotechnol. **34**(10), 810–824 (2016).
6. C. Yu, S. Fan, Y. Sun, and E. Pickwell-MacPherson, "The potential of terahertz imaging for cancer diagnosis: A review of investigations to date," Quant. Imaging Medicine Surg. **2**(1), 33–45 (2012).
7. R. Ceolato, B. Tanguy, C. Martin, T. Huet, P. Chervet, G. Durand, N. Riviere, L. Hespel, N. Diakonova, D. But, W. Knap, J. Meilhan, B. Delplanque, J. Oden, and F. Simoens, "Performance evaluation of active sub-terahertz systems in degraded visual environments (dve)," Proc. SPIE **9839**, 983906 (2016).
8. C. Prophète, R. Pierrat, H. Sik, E. Kling, R. Carminati, and J. de Rosny, "Modeling of an active terahertz imaging system in brownout conditions," Appl. Opt. **57**(21), 6017–6026 (2018).
9. Y. Hu, P. Huang, L. Guo, X. Wang, and C. Zhang, "Terahertz spectroscopic investigations of explosives," Phys. Lett. A **359**(6), 728–732 (2006).
10. K. Kawase, Y. Ogawa, Y. Watanabe, and H. Inoue, "Non-destructive terahertz imaging of illicit drugs using spectral fingerprints," Opt. Express **11**(20), 2549–2554 (2003).
11. L. Yu, L. Hao, T. Meiqiong, H. Jiaoqi, L. Wei, D. Jinying, C. Xueping, F. Weiling, and Z. Yang, "The medical application of terahertz technology in non-invasive detection of cells and tissues: opportunities and challenges," RSC Adv. **9**(17), 9354–9363 (2019).
12. M. Tonouchi, "Cutting-edge terahertz technology," Nat. Photonics **1**(2), 97–105 (2007).
13. B. B. Hu and M. C. Nuss, "Imaging with terahertz waves," Opt. Lett. **20**(16), 1716–1718 (1995).
14. D. M. Mittleman, "Twenty years of terahertz imaging [Invited]," Opt. Express **26**(8), 9417–9431 (2018).
15. H. Guerboukha, K. Nallappan, and M. Skorobogatiy, "Toward real-time terahertz imaging," Adv. Opt. Photonics **10**(4), 843–938 (2018).
16. J. Neu and C. A. Schmuttenmaer, "Tutorial: An introduction to terahertz time domain spectroscopy (thz-tds)," J. Appl. Phys. **124**(23), 231101 (2018).
17. F. Ospald, W. Zouaghi, R. Beigang, C. Matheis, J. Jonuscheit, B. Recur, J.-P. Guillet, P. Mounaix, W. Vleugels, P. V. Bosom, L. V. Gonzalez, I. Lopez, R. M. Edo, Y. Sternberg, and M. Vandewal, "Aeronautics composite material inspection with a terahertz time-domain spectroscopy system," Opt. Eng. **53**(3), 031208 (2013).
18. F. Simoens and J. Meilhan, "Terahertz real-time imaging uncooled array based on antenna- and cavity-coupled bolometers," Philos. Trans. R. Soc., A **372**(2012), 20130111 (2014).
19. A. W. M. Lee, Q. Qin, S. Kumar, B. S. Williams, Q. Hu, and J. L. Reno, "Real-time terahertz imaging over a standoff distance (>25 meters)," Appl. Phys. Lett. **89**(14), 141125 (2006).
20. A. W. M. Lee, B. S. Williams, S. Kumar, Q. Hu, and J. L. Reno, "Real-time imaging using a 4.3-THz quantum cascade laser and a 320 × 240 microbolometer focal-plane array," IEEE Photonics Technol. Lett. **18**(13), 1415–1417 (2006).
21. M. Dyakonov and M. Shur, "Shallow water analogy for a ballistic field effect transistor: New mechanism of plasma wave generation by DC current," Phys. Rev. Lett. **71**(15), 2465–2468 (1993).
22. R. Tauk, F. Teppe, S. Boubanga, D. Coquillat, W. Knap, Y. M. Meziani, C. Gallon, F. Boeuf, T. Skotnicki, C. Fenouillet-Beranger, D. K. Maude, S. Rumyantsev, and M. S. Shur, "Plasma wave detection of terahertz radiation by silicon field effects transistors: Responsivity and noise equivalent power," Appl. Phys. Lett. **89**(25), 253511 (2006).
23. F. Schuster, D. Coquillat, H. Videlier, M. Sakowicz, F. Teppe, L. Dussopt, B. Giffard, T. Skotnicki, and W. Knap, "Broadband terahertz imaging with highly sensitive silicon cmos detectors," Opt. Express **19**(8), 7827–7832 (2011).
24. M. Bauer, R. Venckevičius, I. Kašalynas, S. Boppel, M. Mundt, L. Minkevičius, A. Lisauskas, G. Valušis, V. Krozer, and H. G. Roskos, "Antenna-coupled field-effect transistors for multi-spectral terahertz imaging up to 4.25 THz," Opt. Express **22**(16), 19235–19241 (2014).
25. Z. Zhou, T. Zhou, S. Zhang, Z. Shi, Y. Chen, W. Wan, X. Li, X. Chen, S. N. Gilbert Corder, Z. Fu, L. Chen, Y. Mao, J. Cao, F. G. Omenetto, M. Liu, H. Li, and T. H. Tao, "Multicolor t-ray imaging using multispectral metamaterials," Adv. Sci. **5**(7), 1700982 (2018).
26. M. M. M. Romano, A. Chulkov, A. Sommier, D. L. Balageas, V. Vavilov, J. C. Batsale, and C. Pradère, "Broadband sub-terahertz camera based on photothermal conversion and IR thermography," J. Infrared, Millimeter, Terahertz Waves **37**(5), 448–461 (2016).
27. S. A. Kuznetsov, A. G. Paulish, A. V. Gelfand, P. A. Lazorskiy, and V. N. Fedorinin, "Bolometric thz-to-ir converter for terahertz imaging," Appl. Phys. Lett. **99**(2), 023501 (2011).
28. F. Alves, L. Pimental, D. Grbovic, and G. Karunasiri, "Mems terahertz-to-infrared band converter using frequency selective planar metamaterial," Sci. Rep. **8**(1), 12466 (2018).
29. K. Fan, J. Y. Suen, X. Liu, and W. J. Padilla, "All-dielectric metasurface absorbers for uncooled terahertz imaging," Optica **4**(6), 601–604 (2017).
30. C. Pradere, J.-P. Caumes, D. Balageas, S. Salort, E. Abraham, B. Chassagne, and J.-C. Batsale, "Photothermal converters for quantitative 2d and 3d real-time terahertz imaging," Quant. InfraRed Thermogr. J. **7**(2), 217–235 (2010).

Optics EXPRESS

31. S. A. Kuznetsov, A. G. Paulish, A. V. Gelfand, P. A. Lazorskiy, and V. N. Fedorinin, "Matrix struture of metamaterial absorbers for multispectral terahertz imaging," Prog. Electromagn. Res. **122**, 93–103 (2012).
32. M. Makhsiyan, P. Bouchon, J. Jaeck, J.-L. Pelouard, and R. Haïdar, "Shaping the spatial and spectral emissivity at the diffraction limit," Appl. Phys. Lett. **107**(25), 251103 (2015).
33. P. Bouchon, C. Koechlin, F. Pardo, R. Haïdar, and J.-L. Pelouard, "Wideband omnidirectional infrared absorber with a patchwork of plasmonic nanoantennas," Opt. Lett. **37**(6), 1038–1040 (2012).
34. B. J. Lee, L. P. Wang, and Z. M. Zhang, "Coherent thermal emission by excitation of magnetic polaritons between periodic strips and a metallic film," Opt. Express **16**(15), 11328–11336 (2008).
35. A. Salmon, M. Lavancier, C. Brulon, L. Coudrat, B. Fix, G. Ducournau, R. Peretti, and P. Bouchon, "Rapid prototyping of flexible terahertz metasurfaces using a microplotter," Opt. Express **29**(6), 8617–8625 (2021).
36. M. A. Ordal, R. J. Bell, R. W. Alexander, L. L. Long, and M. R. Querry, "Optical properties of fourteen metals in the infrared and far infrared: Al, Co, Cu, Au, Fe, Pb, Mo, Ni, Pd, Pt, Ag, Ti, V, and W.," Appl. Opt. **24**(24), 4493–4499 (1985).
37. W. Tan, C. Zhang, C. Li, X. Zhou, X. Jia, Z. Feng, J. Su, and B. Jin, "Selective coherent perfect absorption of subradiant mode in ultrathin bi-layer metamaterials via antisymmetric excitation," Appl. Phys. Lett. **110**(18), 181111 (2017).
38. L. Huang, D. R. Chowdhury, S. Ramani, M. T. Reiten, S.-N. Luo, A. K. Azad, A. J. Taylor, and H.-T. Chen, "Impact of resonator geometry and its coupling with ground plane on ultrathin metamaterial perfect absorbers," Appl. Phys. Lett. **101**(10), 101102 (2012).
39. R. T. Ako, A. Upadhyay, W. Withayachumnankul, M. Bhaskaran, and S. Sriram, "Dielectrics for terahertz metasurfaces: Material selection and fabrication techniques," Adv. Opt. Mater. **8**(3), 1900750 (2020).
40. P. D. Cunningham, N. N. Valdes, F. A. Vallejo, L. M. Hayden, B. Polishak, X.-H. Zhou, J. Luo, A. K.-Y. Jen, J. C. Williams, and R. J. Twieg, "Broadband terahertz characterization of the refractive index and absorption of some important polymeric and organic electro-optic materials," J. Appl. Phys. **109**(4), 043505 (2011).
41. B. Kumanek and D. Janas, "Thermal conductivity of carbon nanotube networks: a review," J. Mater. Sci. **54**(10), 7397–7427 (2019).
42. P. Gonnet, Z. Liang, E. S. Choi, R. S. Kadambala, C. Zhang, J. S. Brooks, B. Wang, and L. Kramer, "Thermal conductivity of magnetically aligned carbon nanotube buckypapers and nanocomposites," Curr. Appl. Phys. **6**(1), 119–122 (2006).
43. H.-T. Chen, "Interference theory of metamaterial perfect absorbers," Opt. Express **20**(7), 7165–7172 (2012).
44. X. Zhao, J. Zhang, K. Fan, G. Duan, G. D. Metcalfe, M. Wraback, X. Zhang, and R. D. Averitt, "Nonlinear terahertz metamaterial perfect absorbers using GaAs [Invited]," Photonics Res. **4**(3), A16–A21 (2016).
45. J. Song, L. Lu, B. Li, B. Zhang, R. Hu, X. Zhou, and Q. Cheng, "Thermal routing via near-field radiative heat transfer," Int. J. Heat Mass Transfer **150**, 119346 (2020).